Materials Chemistry and Physics 258 (2021) 123991

Contents lists available at ScienceDirect

Materials Chemistry and Physics

journal homepage: www.elsevier.com/locate/matchemphys

Effect of temperature on ultrasonic spray pyrolysis method in zinc tungstate: The relationship between structural and optical properties

Anderson A.G. Santiago [a,*], Ricardo L. Tranquilin [b], Maximo S. Li [c], Elson Longo [b], Fabiana V. Motta [a], Mauricio R.D. Bomio [a]

[a] LSQM – Laboratory of Chemical Synthesis of Materials – Department of Materials Engineering, Federal University of Rio Grande Do Norte – UFRN, P.O. Box 1524, Natal, RN, Brazil
[b] CDMF-UFSCar, Universidade Federal de São Carlos, P.O. Box 676, 13565-905, São Carlos, SP, Brazil
[c] IFSC, USP, Av. Trabalhador São Carlense, 400, CEP 13566-590, São Carlos, SP, Brazil

HIGHLIGHTS

- $ZnWO_4$ samples were obtained with success by ultrasonic spray pyrolysis.
- Heat treatment modifications provoked structural and morphological alterations.
- Photoluminescence spectra were influenced by change structural.

ARTICLE INFO

Keywords:
Ultrasonic spray pyrolysis
Photoluminescence
Zinc tungstate
Heat treatment

ABSTRACT

Zinc tungstate is an inorganic material which shows immense potential in diverse areas such as photoluminescence, sodium-ion batteries, and catalysis. Thus, the synthesis and characterization of $ZnWO_4$ by ultrasonic spray pyrolysis using different heat treatments (between 750 °C and 1000 °C) is reported herein. X-ray diffraction and Raman spectroscopy were used to confirm the formation of the $ZnWO_4$ with wolframite-type monoclinic structure. Scanning electron microscopy images revealed that the $ZnWO_4$ particles have a microsphere-like morphology formed by the junction of different nanocrystals and its surface changed by heat treatment. The bandgap energies had a small variation among the samples (3.88 eV–3.98 eV). The photoluminescence emission of the samples showed a broadband spectrum with white light, in which structural alterations occurred with the increase in the heat treatment, which also increased the emission intensity and broadband. The samples synthesized at 950 °C and 1000 °C showed to be promising warm- and neutral-white light emission sources.

1. Introduction

Metallic tungstates form a semiconductor category with enormous potential and have been investigated in different areas, as well as for applications in biotransformation, lithium-ion storage capacity, laser hosting, scintillator, photocatalysis, and photoluminescence, for example [1–6]. $ZnWO_4$ is notable among tungstates for its interesting properties such as excellent chemical and thermal characteristics, in addition to optical properties [7,8]. The $ZnWO_4$ structure is constituted by $[ZnO_6]/[WO_6]$ clusters producing a monoclinic lattice and minor cluster distortions stimulate significant alterations in the optical and vibrational response [9,10].

Huang and Zhu [11] studied how changes in temperature and time of the coprecipitation synthesis can enhance the RhB degradation of $ZnWO_4$, in which higher temperatures and times resulted in superior performance. Meanwhile, Hu, Luo, and Yu [12] verified that $ZnWO_4$ synthesized by different concentrations of ethylene glycol (EG) resulted in controlling particle size, imperfect crystallinity, low carrier separation efficacy, and improved photocatalytic removal of pollutants and disinfection of bacteria. However, Harichandran et al. [13] studied the influence of cetyl-trimethylammonium bromide (CTAB) in $ZnWO_4$ particles by the sonochemical method, and observed structural and morphological alterations that resulted in superior specific capacitance value. Furthermore, Wang et al. [14] utilized L-aspartic acid (L-Asp) as a

* Corresponding author.
E-mail address: andersonsantiago@ufrn.edu.br (A.A.G. Santiago).

https://doi.org/10.1016/j.matchemphys.2020.123991
Received 28 May 2020; Received in revised form 17 August 2020; Accepted 26 October 2020
Available online 27 October 2020

surfactant to obtain yolk-shell $ZnWO_4$ microspheres by the hydrothermal method, and observed that the microspheres showed improved optical properties in comparison to nanorods (without L-Asp). Thus, the boost of $ZnWO_4$ performance generally occurs by distortion and imperfection in the clusters, and this can be accomplished by different cation doping, distinct synthesis methods, and the variants [15–17].

Ultrasonic spray pyrolysis (USP) is a method used to obtain ceramic powders with sphere-like morphology easily, simply, and without surfactants due to being a continuous and fast process which allows several modifications in synthesis parameters [18,19]. The alteration of USP parameters can provide substantial changes to the same composite through easy control of residence time, heat treatment, size, and concentration of droplets during the process which will promote morphological, structural, and different properties for the resulting material [20]. $ZnWO_4$ is a material which has been explored by different methods such as state-solid [21], sol-gel [22], microwave-assisted and conventional hydrothermal [15,23,24], as well as sonochemical [13,25], but it has only been little reported in being obtained by USP. Huang et al. [26] and Santiago et al. [27] synthesized $ZnWO_4$ by the USP utilizing thermal processing at 650–750 °C and 800 °C, respectively.

Consequently, further studies are necessary to check the structural and morphological behavior of this material under different conditions during the USP method. Based on the above factors, in this study we present an investigation on the structure, morphology, and optical alterations generated in $ZnWO_4$ powder by the USP method at different temperatures (between 750 °C and 1000 °C).

2. Experimental details

2.1. The synthesis procedure of $ZnWO_4$ powders

The USP process was used to synthesize $ZnWO_4$ samples. First, solution I was prepared with 5 mmol of tungstic acid (H_2WO_4, 99% purity, Aldrich Chemistry) in 25 ml of H_2O, then mixed by a magnetic stirrer at 25 °C and the pH was modified to 12 using ammonium hydroxide (NH_4OH, 30%, Synth), thus obtaining a white and semi-transparent solution. Next, nitric acid (HNO_3, 65%, Synth) was added to solution I to decrease the pH to 5. Solution II was subsequently prepared with 5 mmol of zinc nitrate hexahydrate ($Zn(NO_3)_2 \cdot 6H_2O$, 98% purity, Sigma-Aldrich) in 75 ml of H_2O and mixed by a magnetic stirrer at 25 °C, supporting the pH at 5. Then, solution I was added dropwise into solution II to obtain the precursor solution, with the precursor solution concentration at 0.6313 M. Finally, the precursor solution was atomized using an ultrasonic nebulizer (frequency of 2.4 MHz) with air as carrier gas (flow at 2 L min^{-1}), and the furnace temperature was set to 600 °C for zone 1 and between 750 and 1000 °C for zone 2. The temperature setting in zone 2 for the samples were 750, 800, 850, 900, 950, and 1000 °C, denominated as Z750, Z800, Z850, Z900, Z950 and Z1000, respectively. The precipitates were then collected by an electrostatic stainless-steel precipitator. More information about the equipment and technology used is available in references [28–30].

2.2. Characterization of $ZnWO_4$ powders

Powder XRD patterns of $ZnWO_4$ were collected within the 10° to the 120° angular range with a speed of 1° min^{-1} and step of 0.02° using a Shimadzu diffractometer, model XRD 7000, with monochromatic $Cu_{K\alpha}$ radiation ($\lambda = 1.5406$ Å). The General Structure Analysis System (GSAS) with an EXPGUI graphic interface [31] was used to execute the Rietveld refinement [32] and to obtain structural modifications of samples. Next, a Supra 35-VP Carl Zeiss Field-gun scanning electronic microscope (FE-SEM) operating at 6 kV was used to perform the morphological images. A VERTEX 70 RAMII Bruker spectrophotometer (USA) with an Nd:YAG laser (1024 nm) and maximum output power kept at 100 mW was then used to obtain Raman scattering spectra at room temperature in the frequency range from 100 to 1000 cm^{-1}. A Shimadzu UV-2600 spectrometer was used to obtain the UV–Vis reflectance spectrum. Finally, a thermal Jarrell-Ash Monospec 27 monochromator, a Hamamatsu R446 photomultiplier, and a krypton laser with a wavelength of 325 nm (Coherent Innova) and an output of 5 mW were used to obtain photoluminescence spectra at ambient temperature.

3. Results and discussion

The XRD patterns of $ZnWO_4$ samples are shown in Fig. 1. All the samples have been indexed as wolframite-type monoclinic structure with space group *P2/c* (number 13) in accordance with JCPDS 15–774 and references [33,34], exhibiting great crystallinity, however an improvement in crystallinity and the peak shape definition are noted with increasing temperature.

Fig. 2 and Table 1 show the results achieved by the Rietveld refinement of all samples. All samples were well fitted to ICSD 84540 ($ZnWO_4$ with monoclinic structure). Small alterations are observed in the lattice parameters between samples due to different temperatures used during the USP process, and as a result present a variation in crystallite size and cluster distortions.

The temperature variation changes the heating rate and residence time that droplets and particles experience during the USP process, as the higher temperature implies a high heating rate and low residence time [35]. The residence time was estimated by:

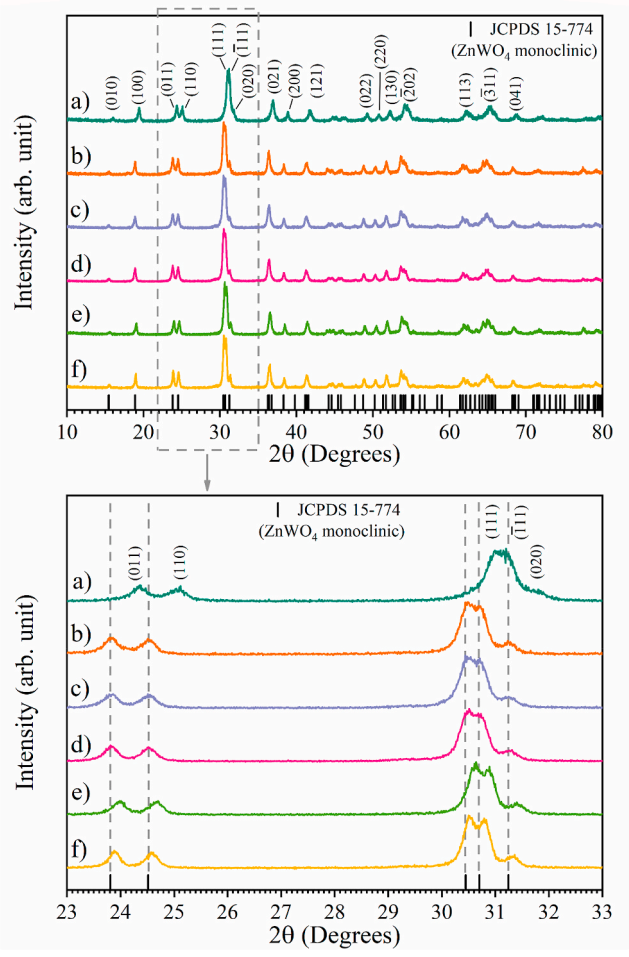

Fig. 1. XRD patterns of $ZnWO_4$ samples obtained by the USP method, namely (a) Z750, (b) Z800, (c) Z850, (d) Z900, (e) Z950, and (f) Z1000. (For interpretation of the references to colour in this figure legend, the reader is referred to the web version of this article.)

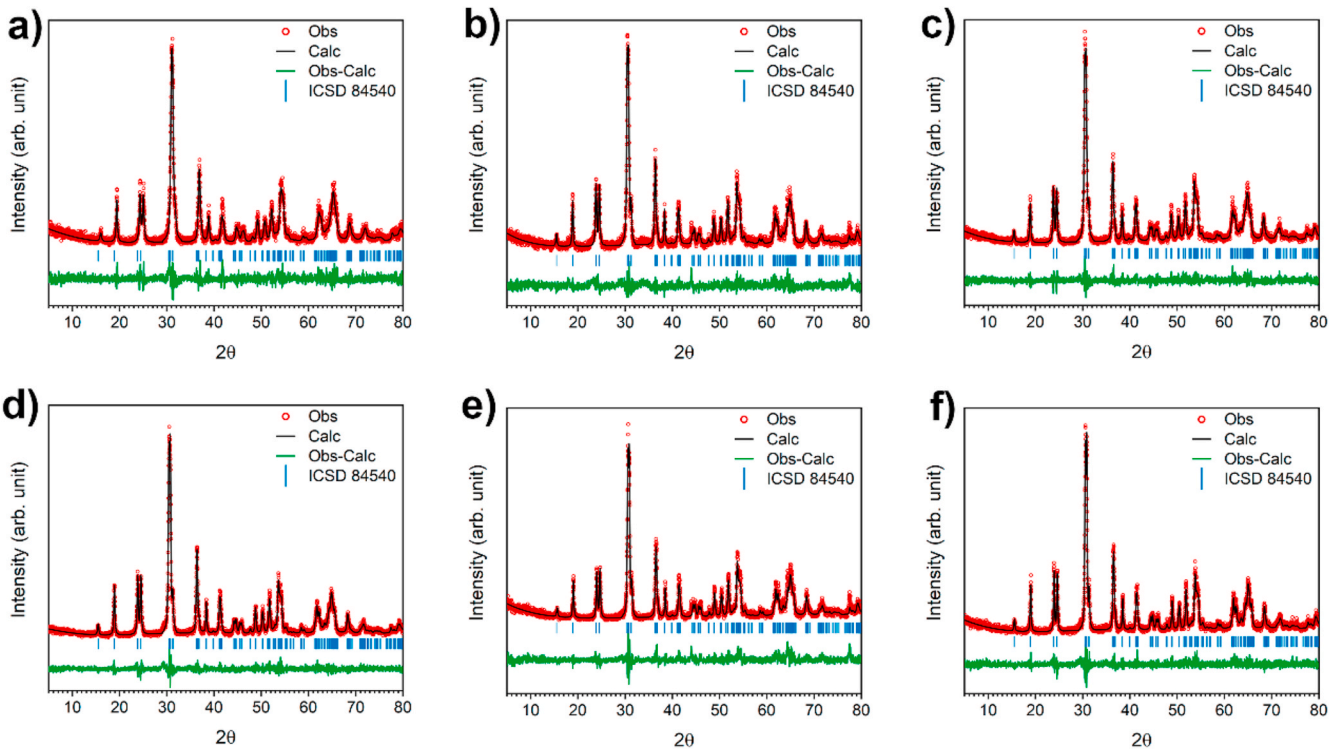

Fig. 2. Rietveld Refinement of $ZnWO_4$ samples, namely (a) Z750, (b) Z800, (c) Z850, (d) Z900, (e) Z950, and (f) Z1000. (For interpretation of the references to colour in this figure legend, the reader is referred to the web version of this article.)

Table 1
Structural parameters, crystallite size, microstrain, and reliability parameters obtained by Rietveld refinement for the $ZnWO_4$ samples.

Compounds	Z750	Z800	Z850	Z900	Z950	Z1000
Crystal system	Monoclinic	Monoclinic	Monoclinic	Monoclinic	Monoclinic	Monoclinic
Space Group	*P2/c*	*P2/c*	*P2/c*	*P2/c*	*P2/c*	*P2/c*
Lattice parameters (Å)						
a	4.697	4.693	4.695	4.693	4.695	4.686
b	5.727	5.719	5.721	5.719	5.721	5.710
c	4.936	4.929	4.929	4.928	4.927	4.916
β	89.37	90.64	90.67	90.68	90.71	90.71
V(Å^3)	132.8	132.3	132.4	132.2	132.2	131.5
χ^2	1.342	1.574	1.358	1.416	1.601	1.300
Rf^2 (%)	7.86	11.82	7.38	6.11	15.53	7.94
Rp (%)	15.34	11.66	10.92	9.57	13.90	11.22
D (nm)	17.3	24.9	23.4	24.9	25.8	27.1
ε (x10^{-3})	1.02	0.71	0.73	0.70	0.68	0.65

$$t_i = \frac{A \times l}{F} \times \frac{T_{room}}{T_i} \quad (1)$$

In which: A is the cross-sectional area of the tube, l is the length of each zone, F is the carrier gas flow rate, T_{room} is the room temperature, and T_i is the temperature in each zone [35,36]. Thus, the calculated residence times were 6.02 s, 5.82 s, 5.64 s, 5.48 s, 5.35 s, and 5.23 s to Z750, Z800, Z850, Z900, Z950 and Z1000, respectively. On the other hand, it is noted that the Z1000 sample had higher crystallinity and improve XRD patterns at lower residence time. Moreover, the crystallite size showed an increase at higher temperatures, while the unit cell volume exhibited a decrease. As can be seen in Table 1, the lattice parameters a, b, and c increased, while β decreased with increasing temperature. Andrade Neto et al. [15] demonstrated that $ZnWO_4$ tends to decrease the unit cell volume with increased synthesis temperature, approaching theoretical values. Thus, the lattice parameters of $ZnWO_4$ tend to decrease, and the crystallite size tends to increase in higher temperatures due to the high heating rate experienced by droplets and particles during the USP synthesis, as more energy is provided for the particles to crystallize, organize, and grow.

The unit cell of $ZnWO_4$ is formed by two clusters in which Zn^{2+} and W^{6+} are coordinated by six bordering oxygen atoms and a distorted octahedral geometry of ZnO_6 and WO_6 [37,38]. Fig. 3 shows the unit cells of $ZnWO_4$ samples where it is possible to see the distortions and stretching between Zn–O and W–O bonds with the variation in temperature. The W–O bond length was measured, and a tendency of elongation and shrinkage of determined bonds was observed with the increase in temperature. Wang et al. [39] observed analog behavior when obtaining $ZnWO_4$ samples, in which the W–O bond lengths calcined at 500 °C were 1.7752 Å, 2.0111 Å and 2.1801 Å, while the W–O bond lengths calcined at 1000 °C were 1.7794 Å, 2.0523 Å and 2.1158 Å.

Raman spectra were measured in the $ZnWO_4$ samples obtained by 750 and 1000 °C and are shown in Fig. 4. Group theory analysis predicts that the wolframite structure of $ZnWO_4$ yields 36 lattice modes at the Γ point ($8A_g + 10B_g + 8A_u + 10B_u$), but only 18 even ($g$) vibrations are Raman-active modes ($8A_g$+$10B_g$) [40]. In our case, 15 modes ($7A_g$ and $8B_g$) of these 18 modes were found. The increase in temperature resulted

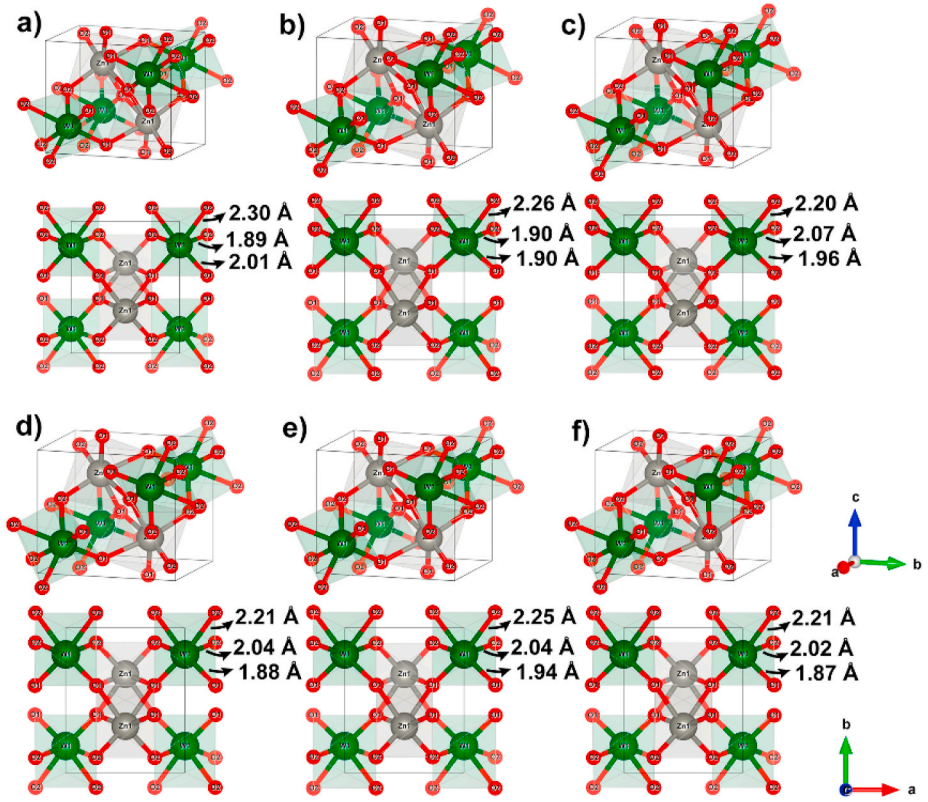

Fig. 3. Unit cells of $ZnWO_4$ samples obtained by USP, namely (a) Z750, (b) Z800, (c) Z850, (d) Z900, (e) Z950, and (f) Z1000. (For interpretation of the references to colour in this figure legend, the reader is referred to the web version of this article.)

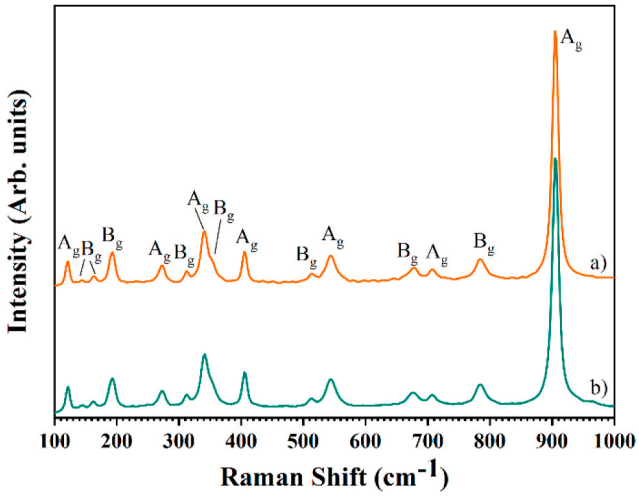

Fig. 4. Raman spectra of $ZnWO_4$ samples obtained by the USP method at (a) 750 °C and (b) 1000 °C. (For interpretation of the references to colour in this figure legend, the reader is referred to the web version of this article.)

in improving the modes' peak shape and the signal-to-noise ratio of the spectrum, which is expected due to the increased crystallization of samples.

The band seen near 904 cm^{-1} is assigned to symmetric stretching of the regular octahedron, while the bands near 785 cm^{-1} and 705 cm^{-1} are assigned to asymmetric stretching of the regular octahedron. The W–*O*–W bridging mode is seen near 513 cm^{-1}, while the bending mode of the regular WO_6 octahedral is seen near 406 cm^{-1}, 341 cm^{-1}, and 193 cm^{-1}. The band near 313 cm^{-1} is assigned to the symmetric stretching of the regular ZnO_6 octahedral, while the band near 272 cm^{-1} and 164 cm^{-1} are assigned to the translational mode of the WO_4 tetrahedral and translational mode of Zn–O, respectively [40,41].

The morphology of $ZnWO_4$ particles was analyzed by FESEM and is shown in Fig. 5. The particles presented a microsphere-like morphology produced by the junction of different nanocrystals (primary nanocrystals), which is expected and commonly observed for the USP method. The particles formed at 750 °C (Fig. 5a) showed a smoother surface and minor primary nanocrystals when compared with the particles formed at 1000 °C (Fig. 5f).

Diverse physicochemical phenomena occur during the USP process which result in the formation of particles, such as the drying up of the solvent on the droplet surface, the dispersion of solvent gases to outside the droplet, and melting of the precursor nitrates. Furthermore, the use of metal nitrates as precursor reagents tend to form porous or hollow microspheres due to its melting before the solvent, thus resulting in a molten salt which prevents the solvent from being completely removed. Moreover, precursor reagents which have high solubility tend to aggregate several nanocrystals to form a microsphere due to high supersaturation, such as what occurs with the metal nitrates [42,43].

Synthesis parameters have a great influence on crystallinity and morphology of produced particles. The temperature influences the heating rate and residence time during the process, as the higher temperature results in higher heating rate, less residence time, increased crystallinity, and higher densification of particles. However, atomization frequency effects droplet size, as the higher frequency results in smaller droplet size and smaller particle size. Nevertheless, the carrier flow gas rate affects residence time, as a high carrier gas rate increases the residence time and promotes the emergence of particles with an irregular surface. Lastly, the precursor solution concentration changes particle size, as low concentration values induce smaller particle sizes [35,42].

The particle formation mechanism can be divided into four main stages (Fig. 5g): the precursor droplet is the carrier in the furnace, which

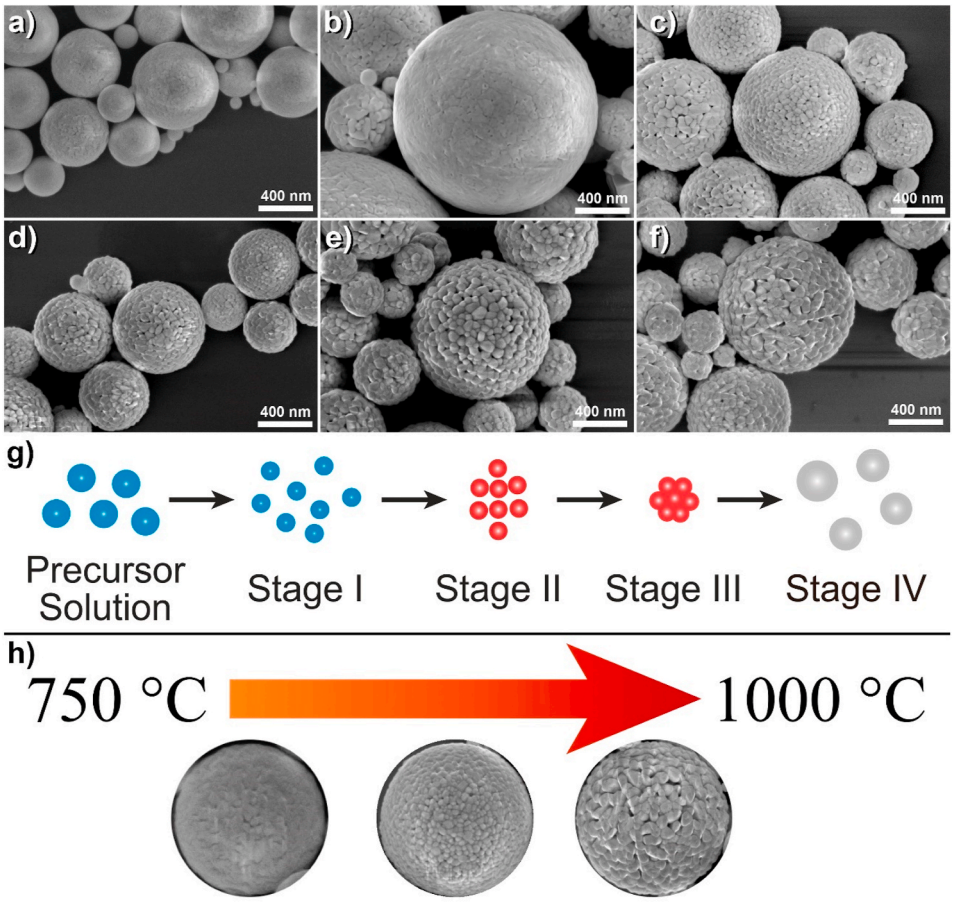

Fig. 5. FESEM images of $ZnWO_4$ particles, namely (a) Z750, (b) Z800, (c) Z850, (d) Z900, (e) Z950, and (f) Z1000. Illustrations of (g) particle formation mechanism and (h) scheme of morphological differences between samples. (For interpretation of the references to colour in this figure legend, the reader is referred to the web version of this article.)

is then heated and evaporation of the solvent from the droplet occurs (Stage I), resulting in a decrease in the precursor droplet diameter and an increase in the precursor concentration; next, the precursor droplet is fully dried and the solute is precipitated (Stage II); the precipitates undergo thermal decomposition and nanocrystals nucleate (Stage III); lastly, the nanocrystals cluster together and grow, resulting in the particles (Stage IV) [20,44].

Thus, the increase in temperature supplies a higher heating rate for nucleation and particle growth, as can be seen in Fig. 5h. The microspheres consequently experience variation in the surface aspect, such as the increase in the roughness and porosity with the increase in temperature due to minor residence time. In our case, the particle surface looked like a melon at 750 °C, and at 1000 °C the surface looked like a sugar-apple.

Fig. 6 shows the band-gap energy of $ZnWO_4$ samples estimated by the Kubelka-Munk function followed by the Wood and Tauc method. The diffuse reflectance data was converted in absorbance by the Kubelka-Munk function [45]. The band-gap energy (E_{gap}) was estimated by the Wood and Tauc method [46] using absorbance data. The optical band-gap energy is assumed by $\alpha h\nu \sim (h\nu\text{-}E_{gap})^{1/k}$ [46], where α is the absorbance, h is the Planck constant, ν is the frequency, and k is indicated for the different kind of transitions. The $ZnWO_4$ is normally related to direct allowed transition [25,47,48], so the results from $ZnWO_4$ powders were examined assuming $k = 1/2$, which is the value for such transitions.

The bandgap values found in the literature are near the values estimated in our samples. The bandgap theoretical value of $ZnWO_4$ was calculated by density-functional theory (DFT) obtaining ~4.019 eV [49]. On the other hand, the experimentally estimated bandgap depends on the synthesis method, synthesis parameters, and doping used to obtain the $ZnWO_4$ samples, as the modified structural parameters result in changes in the bandgap. For example, the value when synthesized by the sol-gel method was 3.20 eV [50], the value by solid-state reaction was 3.93 eV [48], while by microwave-assisted hydrothermal the value was 3.40 eV [51]. The tungstates present two dominant states in the bandgap, being W^{6+}(5 d) states in the conduction band (CB) and O^{2-}(2p) states in the valence band (VB), which are heavily affected by the degree of structural order-disorder due to the low number of intermediate levels in the bandgap [52,53]. The bandgap estimated in our samples had small variation between the samples (3.88–3.98 eV), thus structural modifications with the variation of temperature during the USP method did not strongly influence the bandgap, possibly due to fast heat treatment received by the particles.

The photoluminescence behavior of samples was performed by excitation of 325 nm at ambient temperature and the PL spectra are shown in Fig. 7-I. The PL spectra of samples show a broadband profile, which is characteristic of a multiphonon and multilevel process, i.e. relaxation process which occurs with the participation of numerous energy states within the bandgap of the material [54,55]. The tungstates with monoclinic wolframite-type structure present two clusters, namely $[MO_6]$ and $[WO_6]$ clusters (M = Zn, Mg, Co), but the PL emission occurs by charge transfer in the $[WO_6]$ clusters given by energy absorption through O 2p orbitals and promotion through W 5 d orbitals [24,56]. Moreover, the color emitted by the sample is directly correlated with the structural arrangements and cluster-to-cluster charge transfer of tungstates, wherein the yellow-red emission is related to deep defects,

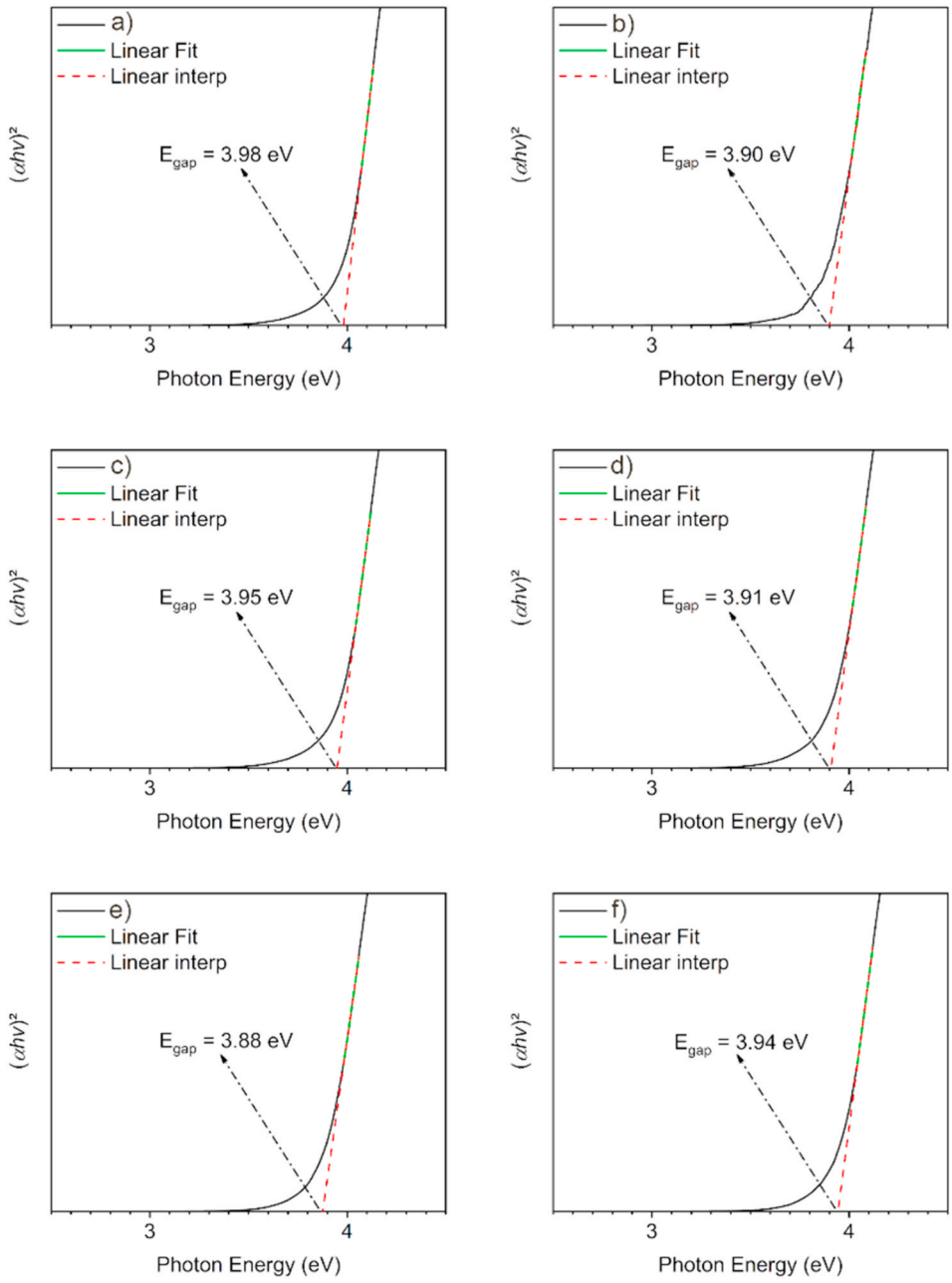

Fig. 6. UV–Vis absorbance spectra of $ZnWO_4$ samples, namely (a) Z750, (b) Z800, (c) Z850, (d) Z900, (e) Z950, and (f) Z1000.

structural disorder and oxygen vacancies in [WO_6] clusters, while the blue-green emission is related to shallow defects and structural ordering [57].

The $ZnWO_4$ samples show an increase of PL intensity and spectrum enlargement to the yellow-red region with an increase in the synthesis temperature up to 950 °C, in which the more intense wavelength is between 490 and 505 nm. On the other hand, the Z1000 sample presented a slight decrease in PL intensity and more intense wavelength at 605 nm. Thus, structural alterations with a high temperature can be promoted to increase deep defects, oxygen vacancies or cluster-to-cluster charge transfer in the $ZnWO_4$ structure. Also, these phenomena can be related to stabilization of the (010) and (011) surfaces with the increase in temperature, which favor the yellow-red emission due to creating oxygen vacancy located in the [$ZnO_4{\cdot}2V_O^x$] and [$WO_5{\cdot}V_O^x$] clusters and provoke the creation of further energy bandgap levels [57,58].

The color emitted by $ZnWO_4$ samples was verified by CIE chromatic (x, y) coordinates and can be seen in Fig. 7II and Table 2. The CIE coordinates and color rendering indices (CRI) are essential indexes to evaluate the performance of matches and the quality of white light sources, respectively. High-quality white light sources should show an emission between neutral- and cool-white color (4000–8000 K) and have CRI values above 80% [59,60]. Several studies have been conducted to obtain high-quality white light sources, and mainly utilized rare earth-like dopants with a ceramics matrix [61–65]. Nevertheless, the use of rare earth can be related to bronchiolar, alveolar, and interstitial histological reactions in the lungs when an individual has prolonged exposure to these elements [66,67]. Thus, the use of materials without rare earth in its composition is important due to health reasons. The structural variations due to changes in temperature of the USP method in our study promoted alteration in CCT and CRI data, with displacement of cool-white to warm-white emission and improvement in the quality CRI occurring. Thus, the Z950 and Z1000 samples can be an alternative for phosphorus application due to having good CCT and CRI

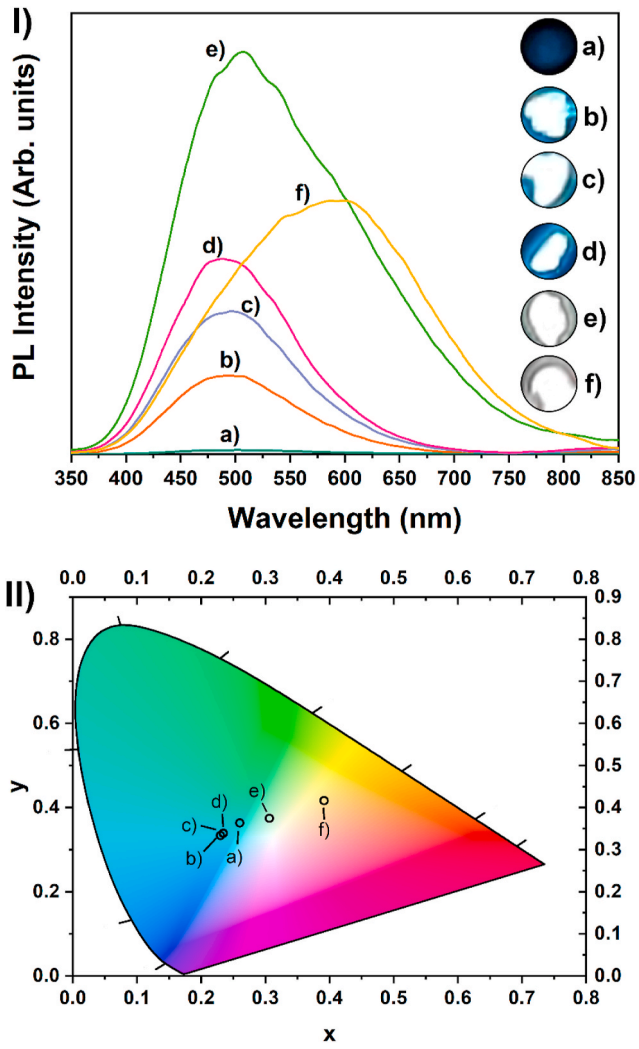

Fig. 7. (I) PL spectra and (II) CIE of $ZnWO_4$ samples, namely (a) Z750, (b) Z800, (c) Z850, (d) Z900, (e) Z950, and (f) Z1000. Inset Fig. 7-I is the picture of PL emission samples during excitation of each sample. (For interpretation of the references to colour in this figure legend, the reader is referred to the web version of this article.)

Table 2
CIE Coordinates, correlation color temperature (CCT), color rendering indices (CRI), and color emission of $ZnWO_4$ samples.

Sample	x	y	CCT (K)	CRI (%)	Color
Z750	0.2602	0.3636	8863	67	Cloudy sky
Z800	0.2345	0.3393	11,531	62	Overcast sky, slightly blue-purple
Z850	0.2343	0.3387	11,599	63	Overcast sky, slightly blue-purple
Z900	0.2301	0.3334	12,338	62	Overcast sky, slightly blue-purple
Z950	0.3063	0.3744	6505	82	Summer sunlight
Z1000	0.3915	0.4165	3994	88	Neutral white

values, as they had emission values near LED commercial lamps (6500 K) and warm/neutral LED lamps (3000–4500 K), respectively.

4. Conclusion

$ZnWO_4$ powders were effectively obtained by the ultrasonic spray pyrolysis method with the temperature between 750 °C and 1000 °C. All XRD patterns showed a wolframite-type monoclinic structure ($ZnWO_4$), Raman spectra showed the modes of $ZnWO_4$, and the particles presented sphere-like morphology. The increase in USP temperature promoted increased crystallinity, decreased unit cell volume, an increase in the Raman spectrum intensity, and growth of primary nanocrystals which form the microspheres. The bandgap of samples had small variations between them (3.88–3.98 eV). The PL spectra of the samples showed broadband with white emission. The structural alterations with the increase in USP temperature may have increased the deep defects, oxygen vacancies or cluster-to-cluster charge transfer in the $ZnWO_4$ structure, and stabilization of the (010) and (011) surfaces, thus can to favor the yellow-red emission due to creating further energy bandgap level. Moreover, the Z950 and Z1000 samples can be considered promising for phosphorus application due to presenting good CCT and CRI values (6505 K/82% and 3994 K/88%, respectively).

CRediT authorship contribution statement

Anderson A.G. Santiago: Methodology, Visualization, Writing - original draft, Visualization. **Ricardo L. Tranquilin:** Investigation. **Maximo S. Li:** Data curation, Resources. **Elson Longo:** Resources. **Fabiana V. Motta:** Supervision. **Mauricio R.D. Bomio:** Writing - review & editing, Project administration.

Declaration of competing interest

The authors declare that they have no known competing financial interests or personal relationships that could have appeared to influence the work reported in this paper.

Acknowledgments

The authors thank the following Brazilian research financing institutions for financial support: A.A.G. Santiago and M.R.D. Bomio acknowledges the financial support from the National Council for Scientific and Technological Development (*CNPq*) – Finance codes (140231/2018–8) and (303657/2017–0), respectively. The Coordination for the Improvement of Higher Education Personnel (CAPES) - Brazil (CAPES) - Finance Code 001 and CAPES/PROCAD 2013/2998/2014 and the Graduate Program in Materials Science and Engineering (*PPGCEM-UFRN*). Sao Paulo Research Foundation – (FAPESP) (Process 2013/07296–2), (2016/23891–6ds).

References

[1] A. Blazevic, M. Albu, S. Mitsche, S.K.R. Rittmann, G. Habler, T. Milojevic, Biotransformation of scheelite $CaWO_4$ by the extreme thermoacidophile metallosphaera sedula: tungsten-microbial interface, Front. Microbiol. 10 (2019) 1492.
[2] P. Belli, R. Bernabei, Y.A. Borovlev, F. Cappella, V. Caracciolo, R. Cerulli, F. A. Danevich, A. Incicchitti, D.V. Kasperovych, O.G. Polischuk, V.N. Shlegel, D. S. Tkachev, S.V. Tkachev, V.I. Tretyak, V.N. Zhdankov, New development of radiopure $ZnWO_4$ crystal scintillators, Nucl. Instrum. Method. A 935 (2019) 89–94.
[3] X. Ren, J. Xie, S. Ruan, X. Wang, J. Pei, L. Yu, H. Yu, H. Zhang, Q. Lv, L. Guo, H. Cao, S. Xie, Y. Gao, B. He, C. Du, Diode-end-pumped solid state $ZnWO_4$ Raman laser at 2254 nm, Laser Phys. 30 (2020), 015001.
[4] R.V. Yadav, R.S. Yadav, A.K. Singh, A. Bahadur, T.P. Yadav, S.B. Rai, Alkali ions effect on optical properties of Tm^{3+}, Yb^{3+} co-doped gadolinium tungstate phosphor, Mater. Chem. Phys. 215 (2018) 277–284.
[5] P.R. Ilango, K. Prasanna, Y.N. Jo, P. Santhoshkumar, C.W. Lee, Wet chemical synthesis and characterization of nanocrystalline $ZnWO_4$ for application in Li-ion batteries, Mater. Chem. Phys. 207 (2018) 367–372.
[6] A.A.G. Santiago, E.M. Macedo, F.K.F. Oliveira, F.V. Motta, M.R.D. Bomio, Synthesis and characterization of $BaWO_4$:xTm^{3+},yPr^{3+} obtained by ultrasonic spray pyrolysis, J. Mater. Sci. Mater. Electron. 31 (2020) 11599–11608.
[7] P. Huo, Y. Tang, M. Zhou, J. Li, Z. Ye, C. Ma, L. Yu, Y. Yan, Fabrication of $ZnWO_4$ -CdS heterostructure photocatalysts for visible light induced degradation of ciprofloxacin antibiotics, J. Ind. Eng. Chem. 37 (2016) 340–346.
[8] G.B. Kumar, K. Sivaiah, S. Buddhudu, Synthesis and characterization of $ZnWO_4$ ceramic powder, Ceram. Int. 36 (2010) 199–202.
[9] A. Kalinko, A. Kuzmin, Static and dynamic structure of $ZnWO_4$ nanoparticles, J. Non-Cryst. Solids 357 (2011) 2595–2599.

[10] M.G. Brik, V. Nagirnyi, M. Kirm, First-principles calculations of the structural, electronic and elastic properties of $ZnWO_4$ and $CdWO_4$ single crystals at the ambient and elevated pressure, Mater. Chem. Phys. 137 (2013) 977–983.

[11] G. Huang, Y. Zhu, Synthesis and photocatalytic performance of $ZnWO_4$ catalyst, Mater. Sci. Eng., B 139 (2007) 201–208.

[12] H. He, Z. Luo, C. Yu, Multifunctional $ZnWO_4$ nanoparticles for photocatalytic removal of pollutants and disinfection of bacteria, J. Photochem. Photobiol., A 401 (2020), 112735.

[13] G. Harichandran, P. Divya, J. Yesuraj, B. Muthuraaman, Sonochemical synthesis of chain-like $ZnWO_4$ nanoarchitectures for high performance supercapacitor electrode application, Mater. Char. 167 (2020), 110490.

[14] M. Wang, Y. Tang, T. Sun, G. Jiang, Y. Shi, Yolk–shell $ZnWO_4$ microspheres: one-pot synthesis, characterization and photocatalytic properties, CrystEngComm 16 (2014) 11035–11041.

[15] N.F.A. Neto, T.B.O. Nunes, M. Li, E. Longo, M.R.D. Bomio, F.V. Motta, Influence of microwave-assisted hydrothermal treatment time on the crystallinity, morphology and optical properties of $ZnWO_4$ nanoparticles: photocatalytic activity, Ceram. Int. 46 (2020) 1766–1774.

[16] J. Han, L. Li, M. Peng, B. Huang, F. Pan, F. Kang, L. Li, J. Wang, B. Lei, Toward Bi^{3+} red luminescence with No visible reabsorption through manageable energy interaction and crystal defect modulation in single Bi^{3+}-doped $ZnWO_4$ crystal, Chem. Mater. 29 (2017) 8412–8424.

[17] M.G. Brik, V. Nagirnyi, M. Kirm, Ab-initio studies of the electronic and optical properties of $ZnWO_4$ and $CdWO_4$ single crystals, Mater. Chem. Phys. 134 (2012) 1113–1120.

[18] W.H. Suh, K.S. Suslick, Magnetic and porous nanospheres from ultrasonic spray pyrolysis, J. Am. Chem. Soc. 127 (2005) 12007–12010.

[19] A.A.G. Santiago, N.F. Andrade Neto, E. Longo, C.A. Paskocimas, F.V. Motta, M.R. D. Bomio, Fast and continuous obtaining of Eu^{3+} doped CeO_2 microspheres by ultrasonic spray pyrolysis: characterization and photocatalytic activity, J. Mater. Sci. Mater. Electron. 30 (2019) 11508–11519.

[20] S.C. Tsai, Y.L. Song, C.S. Tsai, C.C. Yang, W.Y. Chiu, H.M. Lin, Ultrasonic spray pyrolysis for nanoparticles synthesis, J. Mater. Sci. 39 (2004) 3647–3657.

[21] A.R. Phani, M. Passacantando, L. Lozzi, S. Santucci, Structural characterization of bulk ZnWO4 prepared by solid state method, J. Mater. Sci. 35 (2000) 4879–4883.

[22] Y. Wu, S.-c. Zhang, L.-w. Zhang, Y.-f. Zhu, Photocatalytic activity of nanosized ZnWO4 prepared by the sol-gel method, Chem. Res. Chin. Univ. 23 (2007) 465–468.

[23] Z. Liu, J. Tian, D. Zeng, C. Yu, L. Zhu, W. Huang, K. Yang, D. Li, A facile microwave-hydrothermal method to fabricate B doped $ZnWO_4$ nanorods with high crystalline and highly efficient photocatalytic activity, Mater. Res. Bull. 94 (2017) 298–306.

[24] C. Li, X. Du, D. Yue, J. Gao, Z. Wang, Full-color emission based $ZnWO_4$ spherical nanoparticles through doping of rare earth ions, Mater. Lett. 108 (2013) 257–260.

[25] D.P. Dutta, P. Raval, Effect of transition metal ion (Cr^{3+}, Mn^{2+} and Cu^{2+}) doping on the photocatalytic properties of $ZnWO_4$ nanoparticles, J. Photochem. Photobiol., A 357 (2018) 193–200.

[26] Y. Huang, Y. Gao, Q. Zhang, J.-j. Cao, R.-j. Huang, W. Ho, S.C. Lee, Hierarchical porous $ZnWO_4$ microspheres synthesized by ultrasonic spray pyrolysis: characterization, mechanistic and photocatalytic NO removal studies, Appl. Catal., A 515 (2016) 170–178.

[27] A.A.G. Santiago, Y.L.R.L. Fernandes, R.L. Tranquilin, E. Longo, C.A. Paskocimas, F. V. Motta, M.R.D. Bomio, Influence of $Zn_{1-x}Ca_xWO_4$ heterostructures synthesized by spray pyrolysis on photoluminescence property, Ceram. Int. 45 (2019) 23256–23264.

[28] P.N. Medeiros, A.A.G. Santiago, E.A.C. Ferreira, M.S. Li, E. Longo, M.R.D. Bomio, F. V. Motta, Influence Ca-doped $SrIn_2O_4$ powders on photoluminescence property prepared one step by ultrasonic spray pyrolysis, J. Alloys Compd. 747 (2018) 1078–1087.

[29] A.A.G. Santiago, R.L. Tranquilin, P. Botella, F.J. Manjón, D. Errandonea, C. A. Paskocimas, F.V. Motta, M.R.D. Bomio, Spray pyrolysis synthesis and characterization of $Mg_{1-x}Sr_xMoO4$ heterostructure with white light emission, J. Alloys Compd. 813 (2020), 152235.

[30] A.A.G. Santiago, L.X. Lovisa, P.N. Medeiros, M.S. Li, N.L.V. Carreño, E. Longo, C. A. Paskocimas, M.R.D. Bomio, F.V. Motta, Fast and simultaneous doping of $Sr_{0.9-x-y-z}Ca_{0.1}In_2O_4$:($xEu^{3+}$, yTm^{3+}, zTb^{3+}) superstructure by ultrasonic spray pyrolysis, Ultrason. Sonochem. 56 (2019) 14–24.

[31] B.H. Toby, EXPGUI, a graphical user interface for GSAS, J. Appl. Crystallogr. 34 (2001) 210–213.

[32] H.M. Rietveld, A profile refinement method for nuclear and magnetic structures, J. Appl. Crystallogr. 2 (1969) 65–71.

[33] G. He, H. Fan, L. Ma, K. Wang, D. Ding, C. Liu, Z. Wang, Synthesis, characterization and optical properties of nanostructured $ZnWO_4$, Mater. Sci. Semicond. Process. 41 (2016) 404–410.

[34] W. Zhao, X. Song, G. Chen, S. Sun, One-step template-free synthesis of $ZnWO_4$ hollow clusters, J. Mater. Sci. 44 (2009) 3082–3087.

[35] Y. Liang, R. Felix, H. Glicksman, S. Ehrman, Cu-Sn binary metal particle generation by spray pyrolysis, Aerosol Sci. Technol. 51 (2017) 430–442.

[36] H.S. Fogler, Essentials of Chemical Reaction Engineering, Pearson Education, 2010.

[37] M. Li, Q. Meng, S. Li, F. Li, Q. Zhu, B.-N. Kim, J.-G. Li, Photoluminescent and photocatalytic $ZnWO_4$ nanorods via controlled hydrothermal reaction, Ceram. Int. 45 (2019) 10746–10755.

[38] T. Dong, Z. Li, Z. Ding, L. Wu, X. Wang, X. Fu, Characterizations and properties of Eu^{3+}-doped $ZnWO_4$ prepared via a facile self-propagating combustion method, Mater. Res. Bull. 43 (2008) 1694–1701.

[39] L. Wang, Y. Ma, H. Jiang, Q. Wang, C. Ren, X. Kong, J. Shi, J. Wang, Luminescence properties of nano and bulk $ZnWO_4$ and their charge transfer transitions, J. Mater. Chem. C 2 (2014) 4651–4658.

[40] D. Errandonea, F.J. Manjón, N. Garro, P. Rodríguez-Hernández, S. Radescu, A. Mujica, A. Muñoz, C.Y. Tu, Combined Raman scattering and investigation of pressure-induced structural phase transitions in the scintillator $ZnWO_4$, Phys. Rev. B 78 (2008), 054116.

[41] P. Yadav, S.K. Rout, E. Sinha, Correlation between optical properties and environmental parameter of $ZnWO_4$ ceramic using complex chemical bond theory, J. Alloys Compd. 726 (2017) 1014–1023.

[42] G.L. Messing, S.-C. Zhang, G.V. Jayanthi, Ceramic powder synthesis by spray pyrolysis, J. Am. Ceram. Soc. 76 (1993) 2707–2726.

[43] H. Jang, K. Miyasaka, I. Taniguchi, Synthesis and characterization of carbon-modified $Li_2MnP_2O_7$/C composites prepared by spray pyrolysis, J. Mater. Sci. 53 (2018) 9138–9148.

[44] E.A.C. Ferreira, N.F.A. Neto, A.A.G. Santiago, C.A. Paskocimas, M.R.D. Bomio, F. V. Motta, Synthesis and characterization of α-Ag_2MoO_4/β-Ag_2MoO_4 heterostructure obtained by fast and simple ultrasonic spray pyrolysis method at different temperatures, J. Mater. Sci. Mater. Electron. 31 (2020) 4271–4278.

[45] L. Tolvaj, K. Mitsui, D. Varga, Validity limits of Kubelka–Munk theory for DRIFT spectra of photodegraded solid wood, Wood Sci. Technol. 45 (2010) 135–146.

[46] D.L. Wood, J. Tauc, Weak absorption tails in amorphous semiconductors, Phys. Rev. B 5 (1972) 3144–3151.

[47] Z. Kowalski, S.M. Kaczmarek, M. Berkowski, M. Głowacki, Y.A. Zhydachevskii, A. Suchocki, Growth and optical properties of $ZnWO_4$ single crystals pure and doped with Ca and Eu, J. Cryst. Growth 457 (2017) 117–121.

[48] G.-T. Xiong, W. Zhang, Z.-F. Hu, P.-J. Hu, Y.-M. Pan, Z.-Y. Feng, L. Ma, Y.-H. Wang, L. Luo, Photocatalytic activity of $ZnWO_4$ phosphors doped with Li impurities, J. Lumin. 206 (2019) 370–375.

[49] A. Benmakhlouf, D. Errandonea, A. Bouhemadou, A. Bentabet, S. Maabed, M. Bouchenafa, S. Bin-Omran, Ab initio study of the mechanical and electronic properties of scheelite-type XWO_4(X = Ca, Sr, Ba) compounds, Int. J. Mod. Phys. B 31 (2017) 1750086.

[50] M. Rahmani, T. Sedaghat, A facile sol–gel process for synthesis of $ZnWO_4$ nanopartices with enhanced band gap and study of its photocatalytic activity for degradation of methylene blue, J. Inorg. Organomet. Polym. Mater. 29 (2018) 220–228.

[51] K.M. Garadkar, L.A. Ghule, K.B. Sapnar, S.D. Dhole, A facile synthesis of $ZnWO_4$ nanoparticles by microwave assisted technique and its application in photocatalysis, Mater. Res. Bull. 48 (2013) 1105–1109.

[52] M.C. Oliveira, L. Gracia, I.C. Nogueira, M.F.d. Carmo Gurgel, J.M.R. Mercury, E. Longo, J. Andrés, Synthesis and morphological transformation of $BaWO_4$ crystals: experimental and theoretical insights, Ceram. Int. 42 (2016) 10913–10921.

[53] L.S. Cavalcante, V.M. Longo, J.C. Sczancoski, M.A.P. Almeida, A.A. Batista, J. A. Varela, M.O. Orlandi, E. Longo, M.S. Li, Electronic structure, growth mechanism and photoluminescence of $CaWO_4$ crystals, CrystEngComm 14 (2012) 853–868.

[54] V.M. Longo, L.S. Cavalcante, A.T. de Figueiredo, L.P.S. Santos, E. Longo, J. A. Varela, J.R. Sambrano, C.A. Paskocimas, F.S. De Vicente, A.C. Hernandes, Highly intense violet-blue light emission at room temperature in structurally disordered $SrZrO_3$ powders, Appl. Phys. Lett. 90 (2007), 091906.

[55] A.A.G. Santiago, C.R.R. Almeida, R.L. Tranquilin, R.M. Nascimento, C. A. Paskocimas, E. Longo, F.V. Motta, M.R.D. Bomio, Photoluminescent properties of the $Ba_{1-x}Zn_xMoO_4$ heterostructure obtained by ultrasonic spray pyrolysis, Ceram. Int. 44 (2018) 3775–3786.

[56] Z. Amouzegar, R. Naghizadeh, H.R. Rezaie, M. Ghahari, M. Aminzare, Microwave engineering of $ZnWO_4$ nanostructures: towards morphologically favorable structures for photocatalytic activity, Ceram. Int. 41 (2015) 8352–8359.

[57] S. Pereira Wda, M.M. Ferrer, G. Botelho, L. Gracia, I.C. Nogueira, I.M. Pinatti, I. L. Rosa, A. La Porta Fde, J. Andres, E. Longo, Effects of chemical substitution on the structural and optical properties of alpha-$Ag_{2-2x}Ni_xWO_4$ (0 </= x </= 0.08) solid solutions, Phys. Chem. Chem. Phys. 18 (2016) 21966–21975.

[58] P.F.S. Pereira, A.F. Gouveia, M. Assis, R.C. de Oliveira, I.M. Pinatti, M. Penha, R. F. Goncalves, L. Gracia, J. Andres, E. Longo, $ZnWO_4$ nanocrystals: synthesis, morphology, photoluminescence and photocatalytic properties, Phys. Chem. Chem. Phys. 20 (2018) 1923–1937.

[59] A.A. Setlur, E.V. Radkov, C.S. Henderson, J.-H. Her, A.M. Srivastava, N. Karkada, M.S. Kishore, N.P. Kumar, D. Aesram, A. Deshpande, B. Kolodin, L.S. Grigorov, U. Happek, Energy-Efficient, high-color-rendering LED lamps using oxyfluoride and fluoride phosphors, Chem. Mater. 22 (2010) 4076–4082.

[60] S. Nizamoglu, G. Zengin, H.V. Demir, Color-converting combinations of nanocrystal emitters for warm-white light generation with high color rendering index, Appl. Phys. Lett. 92 (2008), 031102.

[61] Y. Ke, B. Zhao, K. Ding, Y. Wang, S. Shu, B. Deng, G. Wang, R. Yu, Orange-red-emitting Sm^{3+}-doped double perovskite $CaY_{0.5}Ta_{0.5}O_3$ phosphor with highly thermal stability for white LED applications, J. Lumin. 221 (2020), 116997.

[62] S.A. Khan, A. Jalil, Q. Ullah Khan, R.M. Irfan, I. Mehmood, K. Khan, M. Kiani, B. Dong, N.Z. Khan, J.-L. Yu, L. Zhu, S. Agathopoulos, New physical insight into crystal structure, luminescence and optical properties of YPO_4:Dy^{3+}\$Eu^{3+}$\$Tb^{3+}$ single-phase white-light-emitting phosphors, J. Alloys Compd. 817 (2020), 152687.

[63] X. Yang, Y. Zhang, X. Zhang, J. Chen, H. Huang, D. Wang, X. Chai, G. Xie, M. S. Molokeev, H. Zhang, Y. Liu, B. Lei, Facile synthesis of the desired red phosphor $Li_2Ca_2Mg_2Si_2N_6$:Eu^{2+} for high CRI white LEDs and plant growth LED device, J. Am. Ceram. Soc. 103 (2019) 1773–1781.

[64] P. Balakrishnan, M. Jayachandiran, S.M.M. Kennedy, Color tunable emission from single-phased $Ba_2CaZn_2Si_6O_{17}$: Bi^{3+}, Eu^{3+} phosphors with good energy transfer efficiency for white light emitting diodes, J. Lumin. 215 (2019), 116649.
[65] W. Ran, Q. Wang, Y. Zhou, S. Ding, J. Shi, J.H. Jeong, Fabrication of $ZnWO_4$:Sm^{3+}, Bi^{3+}, Li^{+} with tunable white light-emitting properties for W-LEDs, Mater. Res. Bull. 64 (2015) 146–150.
[66] S. Das, P. Reed McDonagh, T. Selvan Sakthivel, S. Barkam, K. Killion, J. Ortiz, S. Saraf, A. Kumar, A. Gupta, J. Zweit, S. Seal, Tissue deposition and toxicological effects of commercially significant rare earth oxide nanomaterials: material and physical properties, Environ. Toxicol. 32 (2017) 904–917.
[67] K.T. Rim, K.H. Koo, J.S. Park, Toxicological evaluations of rare earths and their health impacts to workers: a literature review, Saf. Health Work. 4 (2013) 12–26.